

IR diagnostics of embedded jets: kinematics and physical characteristics of the HH46-47 jet[★]

R. Garcia Lopez¹, B. Nisini¹, J. Eisloffel², T. Giannini¹, F. Bacciotti³, and L. Podio⁴

¹ INAF-Osservatorio Astronomico di Roma, via di Frascati 33, 00040 Monteporzio Catone, Italy
e-mail: garcia@oa-roma.inaf.it

² Thüringer Landessternwarte Tautenburg, Sternwarte 5, 07778 Tautenburg, Germany

³ INAF-Osservatorio Astrofisico di Arcetri, Largo E. Fermi 5, 50125 Florence, Italy

⁴ Dublin Institute for Advanced Studies, 31 Fitzwilliam Place, Dublin 2, Ireland

Received 16 September 2009 / Accepted 6 December 2009

ABSTRACT

Context. We present an analysis of the kinematics and physical properties of the Class I driven jet HH46-47 based on IR medium and low resolution spectroscopy obtained with ISAAC on VLT.

Aims. Our aim is to study the gas physics as a function of the velocity and distance from the source and to compare the results with similar studies performed on other Class I and classical T Tauri jets as well as with existing models for the jet formation and excitation.

Methods. The ratios and luminosities of several important diagnostic lines (e.g. [Fe II] 1.644, 1.600 μm , [P II] 1.189 μm , and H₂ lines) have been used to derive physical parameters such as electron density, H₂ temperature, iron gas-phase abundance and mass flux. [Fe II] 1.644 μm and H₂ 2.122 μm position velocity diagrams (PVDs) have been additionally constructed to study the kinematics of both the atomic and molecular gas.

Results. Within 1000–2000 AU from the source the atomic gas presents a wide range of radial velocities, from \sim –230 km s^{–1} to \sim 100 km s^{–1}. Only the gas component at the highest velocity (high velocity component, HVC) survives at large distances. The H₂ shows only a single velocity component at almost zero velocity close to the source while it reaches higher velocities (up to \sim 95 km s^{–1}) further downstream. Electron densities (n_e) and mass ejection fluxes (\dot{M}_{jet}) have been separately measured for the HVC and for the component at lower velocity (LVC) from the [Fe II] lines. n_e increases with decreasing velocities with an average value of \sim 6000 cm^{–3} for the LVC and \sim 4000 cm^{–3} for the HVC, while the opposite occurs for \dot{M}_{jet} which is \sim 0.5–2 \times 10^{–7} M_⊙ yr^{–1} and \sim 0.5–3.6 \times 10^{–8} M_⊙ yr^{–1} for the HVC and LVC, respectively. The mass flux carried out by the molecular component, measured from the H₂ lines flux, is \sim 4 \times 10^{–9} M_⊙ yr^{–1}. We have estimated that the Fe gas phase abundance is significantly lower than the solar value, with \sim 88% of iron still depleted onto dust grains in the internal jet region. This fraction decreases to \sim 58%, in the external knots.

Conclusions. Many of the derived properties of the HH46-47 jet are common to jets from young stellar objects (YSOs) in different evolutionary states. The derived densities and mass flux values are typical of Class I objects or very active T Tauri stars. However, the spatial extent of the LVC and the velocity dependence of the electron density have been so far observed only in another Class I jet, the HH34 jet, and are not explained by the current models of jet launching.

Key words. circumstellar matter – Herbig-Haro objects – ISM: jets and outflows – ISM: individual objects: HH46-47 – infrared: ISM

1. Introduction

Protostellar jets are tightly associated with the first stage of protostar evolution. They are believed to remove angular momentum, disrupt infalling material from the cloud, inject turbulence in the ISM and modify its chemistry. Little is known, however, about the origin of protostellar jets. There are two principal schools of thought regarding where protostellar jets are launched from: the X-wind and the disc-wind models (Shu et al. 1995; Ferreira 1997). While disc-wind models assume ejection from a large spread of radii from the disc, X-wind models assume that the ejection of material takes place only at a single annulus at the interaction region between the stellar magnetosphere and the inner edge of the disc. Both models were born in an attempt to explain the kinematical and physical properties observed at optical wavelengths in jets from classical T Tauri stars (e.g., Bacciotti et al. 2000; Lavalley et al. 1997). Very few studies have been done though regarding the physical properties of Class I jets.

Since these objects are still highly embedded in their molecular clouds, they are affected by a large extinction. Thus it is not possible to detect the region near to the exciting source at optical wavelengths. In this context, infrared spectroscopy is a very useful tool to probe the physical properties and kinematics of Class I jets close to their base, where their characteristics have not yet been modified by the interaction with the surrounding material. Several studies have been carried out in recent years employing near-IR (NIR) line diagnostic on protostellar jets (e.g., Nisini et al. 2005; Podio et al. 2006; Davis et al. 2006; Takami et al. 2006). The main lines used to probe physical and kinematical properties in NIR are [Fe II] (e.g. 1.644 μm , 1.600 μm) and H₂ lines (e.g. 2.122 μm). These studies revealed that the kinematical structure at the jet base of Class I and classical T Tauri stars (CTTSs) jets is very similar. Both show a broad line emission near the source which consists of a collimated and large scale jet at high velocity (the so-called HVC) and a slower velocity component (the so-called LVC) that is only detected around the central source. Noticeably, this kind of velocity structure is often observed in both the atomic and molecular components of

[★] Based on observations collected at the European Southern Observatory, Paranal, Chile (ESO programmes 0.74.C-0286(A)).

the jets, the latter probed through the H₂ emission and called molecular hydrogen emission line regions (MHEL; Davis et al. 2001b). Concerning the physical properties, Class I jets show higher densities and mass loss rates than CTTS jets, as expected for less evolved objects. Both disc-wind and X-wind models predict the presence of a large spread of velocity at the jet base as shown by the few synthetic position velocity diagrams (PVDs) constructed for both models (Shang et al. 1998; Pesenti et al. 2004), although attempts to reproduce the specific characteristics (e.g. kinematics, presence of the MHEL region, physical parameters) displayed by the Class I jets are still lacking. We have now started a project aimed to determine a few basic physical parameters of embedded jets as a function of both velocity and distance from the driving source, using near-IR (NIR) medium resolution ($R \sim 10\,000$) spectra taken with ISAAC on the Very Large Telescope (VLT). The goals of this study are to make a quantitative comparison between the physical properties of Class I and CTTS jets and to constrain the origin of the different velocity components and the mechanism responsible for their excitation. In a previous paper (García Lopez et al. 2008), we have applied our NIR diagnostic techniques to two jets, HH34 and HH1.

We now extend this previous study to the HH46-47 jet. This known Class I jet is at a distance of ~ 450 pc emerging from a dense reflecting nebula. The jet is located at the border of a Bok globule and powers an atomic and molecular bipolar flow. The driving source (HH46-IRS) is in a phase of high accretion (Antoniucci et al. 2008) and is known to be a deeply embedded binary system (Reipurth et al. 2000). The northeastern (blue-shifted) portion of the flow is detected at optical wavelengths giving rise to strong HH objects (Hartigan et al. 1993, 2005). Recently, the kinematics of the internal region of this optical jet have been studied in detail by Nishikawa et al. (2008). At infrared wavelengths, the HH46 jet and its red-shifted counter-jet are detected down to the central source (Eislöffel et al. 1994), thus this object represents a very suitable target for our NIR spectroscopy study.

In Sect. 2 we present the observations and the data reduction. In Sect. 3 we describe the results of our observations, while the kinematics of the atomic and molecular components are presented in Sect. 4. In Sects. 5 and 6 we describe the spectral diagnostic analysis applied to ISAAC spectra obtained at low and medium resolution, respectively. We have compared the results found on the HH46-47 jet with the HH34 jet in Sect. 7, and the main conclusions of our work are finally summarised in Sect. 8.

2. Observations and data reduction

The observations were made on 29–30 December 2004 at the ESO VLT telescope on Cerro Paranal, Chile, using the infrared spectrograph and camera ISAAC. The spatial scale of the instrument is $0''.148/\text{pixel}$. We have taken low resolution spectra in the *J*-band ($1.1\text{--}1.4\ \mu\text{m}$) and both medium and low resolution spectra in the *H* ($1.42\text{--}1.82\ \mu\text{m}$) and *K* ($1.82\text{--}2.5\ \mu\text{m}$) bands. The adopted slit widths were $0''.6$ and $0''.3$ for the low and medium resolution, respectively, corresponding to nominal resolutions of 860 (in *J*), 840 (in *H*) and 750 (in *K*) at low resolution (LR) and 10 000 (in *H*) and 8900 (in *K*) at medium resolution (MR). The slits were all aligned along the jet, with a position angle (PA) of $\sim 57^\circ$. Total integration times were 600 s for each filter in the LR mode and 3600 s and 7200 s for the *K*- and *H*-band in the MR mode.

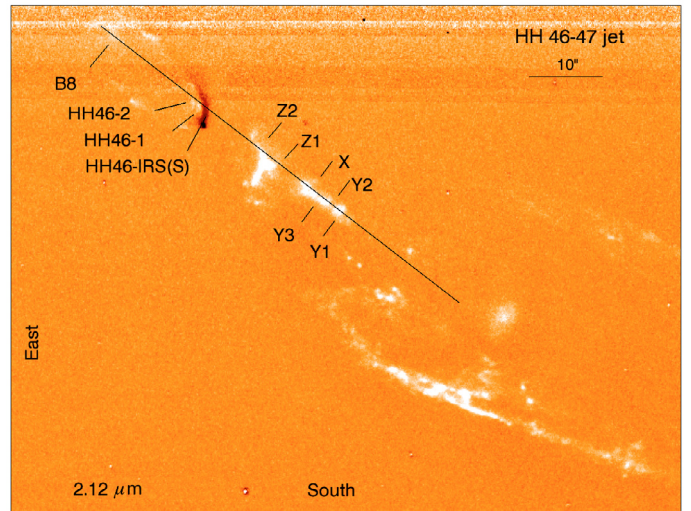


Fig. 1. Position of the ISAAC slit superimposed on the H₂ 2.12 μm image of the HH46-47 jet. At the source (HH46-IRS) and knot S position a negative residual from the continuum subtraction is present. Individual knots along the jet are identified following and our own (see text) nomenclature and that of Eislöffel & Mundt (1994). The northeastern knots correspond to the blue-shifted jet.

Data reduction was performed using standard IRAF¹ tasks. Wavelength calibration was done using the atmospheric OH emission at MR and an argon lamp at LR. The atmospheric spectral response was corrected by dividing the object spectra by the spectrum of a telluric standard star for both modes. Flux calibrations were performed using photometric standards observed at an air mass and seeing similar to our target observations. This procedure probably leads to some flux losses due to the finite slit width with respect to the jet width, especially in the case of the bow shaped knot Z1. In MR spectroscopy, the continuum of the HH46-IRS source was subtracted using the IRAF task BACKGROUND.

The reduced MR spectra on the source position have been already presented in Antoniucci et al. (2008) (reduced and analysed in the same way as explained above) and thus they will not be discussed in the present paper.

3. Results

Figure 1 shows an H₂ 2.12 μm continuum-subtracted image of the HH46-47 jet. The slit position is depicted over the image and the covered knots are named following the nomenclature of Eislöffel & Mundt (1994). In addition, we name as knot S the emission that peaks at the source position and extends for $\sim 3''$ in the blue-shifted jet. The observations cover the blue-shifted jet knots HH46-1 and 2 and the knot B8, which is located at the apex of a bow shock. In the red-shifted lobe, the slit comprises knots Z and Y in Eislöffel & Mundt (1994) that have been separated here in knots Z1 and Z2 and Y1, Y2 and Y3.

The low resolution spectra present several lines of both atomic and molecular species in the different knots. Figure 2 shows the complete spectrum of knot Z1, which is among the brightest ones along the jet. A list of the observed lines, fluxes and identification in knot Z1 is also reported in Table 1, while

¹ IRAF (Image Reduction and Analysis Facility) is distributed by the National Optical Astronomy Observatories, which are operated by AURA, Inc., cooperative agreement with the National Science Foundation.

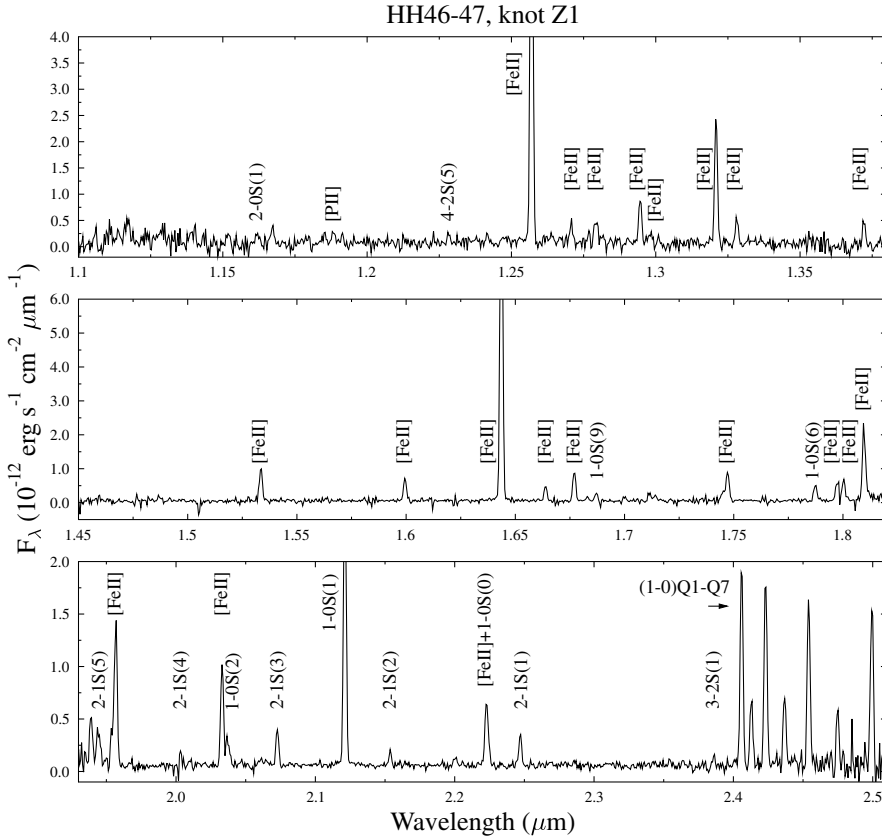


Fig. 2. LR spectrum from 1.00 to 2.50 μm of the knot Z1 in the HH46-47 jet. The strongest lines are identified.

Tables A.1 and A.2 in the Appendix A list all the lines detected in the other knots. [Fe II] transitions from the first 12 fine-structure levels and H₂ transitions from the two first vibrational levels have been detected in all of the knots at various intensity levels. The knot S is together with the knot Z1 the richest in ionic lines. Here [P II] ³P₂ -¹D₂ 1.189 μm has also been detected.

The medium resolution K-band spectra show several lines, the brightest being H₂ 1-0S(1), 3-2S(4) and 2-1S(2), [Fe II] 2.1349 and 2.1609 μm and Br γ (see, Fig. 3). In addition, the [Fe II] 1.600 and 1.644 μm lines have been detected in the H-band spectra. The presence of the Br γ near the source and the H₂ 3-2S(4) line at a distance of 10'' to 25'' from HH46-IRS testifies to the high excitation conditions in these regions. In addition, the on-source spectrum shows other features, as the Br14 and Br12 and CO transitions (see also, Antonucci et al. 2008).

4. Kinematics

In order to study the kinematics of the atomic and molecular component of the HH46-47 jet as a function of distance from the central source, we have constructed PVDs of the [Fe II] 1.644 μm and H₂ 2.122 μm lines (see Fig. 5) from the MR spectral images. The velocity has been expressed with respect to the local standard of rest (LSR) and corrected for a parental cloud velocity of +20 km s⁻¹ (Hartigan et al. 1993). In the Y-axis the distance from the driving source HH46-IRS is represented in arcsec. The continuum of the source has been subtracted in both the PVDs to see the structure of the lines near HH46-IRS more clearly. The intensity scale is different in the two PVDs to show the different condensations in the atomic and molecular gas.

Emission down to the central source is detected for both the atomic and molecular components (knot S). The [Fe II] emission broadens as it approaches the source position and spans velocities

from ~ -200 km s⁻¹ down to 0 km s⁻¹ within 2'' from the source. Inside 1'' there is also emission at red-shifted velocities up to $\sim +100$ km s⁻¹. We will call the blue-shifted component at high velocity, which can be traced up to large scale the high velocity component (HVC) and the more compact emission component from ~ -150 km s⁻¹ to ~ 0 km s⁻¹ the low velocity component (LVC). These two components have been also evidenced in H α optical observations (Nishikawa et al. 2008). At variance with the ionic emission, the H₂ emission close to the source (knot S) shows only one component at nearly 0 km s⁻¹.

The radial velocities of the [Fe II] 1.644 μm and H₂ 2.122 μm lines are reported in Table 2. They have been computed by a Gaussian fit to the line profile of every knot. The velocities of the [Fe II] emission range from -235 km s⁻¹ to -177 km s⁻¹ and from $+144$ km s⁻¹ to $+94$ km s⁻¹ in the blue- and red-lobes, respectively: thus in both lobes the peak velocity decreases as the distance from the driving source increases in both lobes. The HVC and LVC in knot S peak at -213 km s⁻¹ and around -138 km s⁻¹. At knot Z2 the emission splits into two separate velocity components (at $+144$ km s⁻¹ and $+92$ km s⁻¹) whose origin is likely connected with the presence of the large bow shock structure.

The radial velocities of the H₂ emission vary from -15 km s⁻¹ to -48 km s⁻¹ in the blue-lobe and from $+26$ km s⁻¹ to $+94$ km s⁻¹ in the red-lobe. At variance with the [Fe II] emission, knot S only shows a single velocity component at -15 km s⁻¹, while both knots Z1 and X present two velocity components at $\sim +90$ km s⁻¹ and $+10$ km s⁻¹. The high and low velocity components present in these knots and the broad profiles seen in H₂ (see, Fig. 4) are similar to the profiles observed in other molecular jets (e.g., Davis et al. 2001a). As shown in Fig. 4, the relative contribution of the high and low velocities components to the total flux changes from knot Z1 (where the

Table 1. Lines observed in the knot Z1 of the HH46-47 jet.

Line id.	λ (μm)	F (10^{-16} erg cm^{-2} s^{-1})	ΔF	Line id.	λ (μm)	F (10^{-16} erg cm^{-2} s^{-1})	ΔF
[Ti II] $^2\text{G}_{7/2}$ – $^4\text{F}_{7/2}$	1.140	8.3	3.5	H ₂ 1–0 S(6)	1.788	9.4	0.5
H ₂ 2–0 S(1)	1.162	5.8	2.2	[Fe II] $\text{a}^4\text{D}_{3/2}$ – $\text{a}^4\text{F}_{3/2}$	1.797	9.8	1.1
[P II] $^3\text{P}_2$ – $^1\text{D}_2$	1.188	3.5	1.0	[Fe II] $\text{a}^4\text{D}_{5/2}$ – $\text{a}^4\text{F}_{5/2}$	1.800	7.1	0.8
[Fe II] $\text{a}^4\text{D}_{7/2}$ – $\text{a}^6\text{D}_{9/2}$	1.257	106.0	0.8	[Fe II] $\text{a}^4\text{D}_{7/2}$ – $\text{a}^4\text{F}_{7/2}$	1.810	38.2	2.1
[Fe II] $\text{a}^4\text{D}_{1/2}$ – $\text{a}^6\text{D}_{1/2}$	1.271	5.9	1.0	H ₂ 2–1 S(5)	1.945	11.0	1.5
[Fe II] $\text{a}^4\text{D}_{3/2}$ – $\text{a}^6\text{D}_{3/2}$	1.279	7.8	0.1	H ₂ 2–1 S(4)	2.004	2.7	0.3
[Fe II] $\text{a}^4\text{D}_{5/2}$ – $\text{a}^6\text{D}_{5/2}$	1.295	11.9	0.9	H ₂ 1–0 S(2)	2.034	26.1	0.6
[Fe II] $\text{a}^4\text{D}_{3/2}$ – $\text{a}^6\text{D}_{1/2}$	1.298	6.7	0.1	H ₂ 2–1 S(3)	2.074	8.1	0.5
[Fe II] $\text{a}^4\text{D}_{7/2}$ – $\text{a}^6\text{D}_{7/2}$	1.321	306.0	0.8	H ₂ 1–0 S(1)	2.122	68.5	0.3
[Fe II] $\text{a}^4\text{D}_{5/2}$ – $\text{a}^6\text{D}_{3/2}$	1.328	8.4	0.9	H ₂ 2–1 S(2)	2.154	3.9	0.3
[Fe II] $\text{a}^4\text{D}_{7/2}$ – $\text{a}^6\text{D}_{5/2}$	1.372	71.7	1.0	H ₂ 2–1 S(1)	2.248	8.5	0.5
[Fe II] $\text{a}^4\text{D}_{5/2}$ – $\text{a}^4\text{F}_{9/2}$	1.534	173.0	0.7	H ₂ 3–2 S(1)	2.386	1.6	0.4
[Fe II] $\text{a}^4\text{D}_{3/2}$ – $\text{a}^4\text{F}_{7/2}$	1.600	10.6	0.5	H ₂ 1–0 Q(1)	2.407	50.0	0.8
[Fe II] $\text{a}^4\text{D}_{7/2}$ – $\text{a}^4\text{F}_{9/2}$	1.644	160.0	0.6	H ₂ 1–0 Q(2)	2.413	18.3	0.9
[Fe II] $\text{a}^4\text{D}_{1/2}$ – $\text{a}^4\text{F}_{5/2}$	1.664	7.0	0.7	H ₂ 1–0 Q(3)	2.424	47.4	0.9
[Fe II] $\text{a}^4\text{D}_{5/2}$ – $\text{a}^4\text{F}_{7/2}$	1.677	142.0	0.3	H ₂ 1–0 Q(4)	2.437	18.9	1.3
H ₂ 1–0 S(9)	1.687	4.2	0.5	H ₂ 1–0 Q(5)	2.455	42.9	1.5
[Fe II] $\text{a}^4\text{D}_{3/2}$ – $\text{a}^4\text{F}_{5/2}$	1.712	2.1	0.4	H ₂ 1–0 Q(5)	2.455	42.9	1.5
[Fe II] $\text{a}^4\text{D}_{1/2}$ – $\text{a}^4\text{F}_{3/2}$ ^{2*}	1.745	6.3	0.8	H ₂ 1–0 Q(7)	2.500	47.4	3.7
H ₂ 1–0 S(7) ^{3*}	1.748	150.0	0.6				

Notes. (*) Blend of the two indicated lines.

Table 2. Observed radial velocities along the HH46-47 jet.

Knot	[Fe II] 1.644 μm $v(\text{km s}^{-1})$	H ₂ 2.122 μm $v(\text{km s}^{-1})$
B8	–177	
HH46-1	–235	–20
S	–213, (–138)	–15
Z2	+144, +92	+26
Z1	+112	+89, +10
X	+94	+93, +14
Y3		+94
Y2		+92
Y1		+92

Notes. Radial velocities corrected from a cloud velocity of +20 km s^{-1} (Hartigan et al. 1993) and with respect to the LSR. The radial velocity error is 2 km s^{-1} .

component at 0 km s^{-1} is larger than that at high velocity) to knot X (where the component at 0 km s^{-1} is significantly reduced). These profiles are similar to those expected from bow-shock structures viewed at a certain inclination angle (Schultz et al. 2005). With respect to the Schultz et al. (2005) models, the HVC and LVC contribution to the total flux depend in our case not only on the viewing angle of the bow-shock, but also on how the H₂ cooling is distributed from the apex to the wings of the bow. In particular the profiles of the knots Z1 and X are consistent with bow-shocks seen at 30° with respect to the line of sight, but with a different relative contribution to the H₂ cooling between the apex and the wing. In knot X the apex mostly contributes to the total flux, while in knot Z1 the situation is the opposite. Such an effect could be actually due to a poor alignment of the slit with the bow-shock apex in knot Z1.

5. Low resolution spectral analysis

5.1. Extinction

Visual extinction values can be derived from the [Fe II] 1.644/1.257 μm ratio: these lines share the same upper level, and thus their theoretical ratio is a function of the frequencies and probabilities of the transition and is independent of the plasma conditions. To convert the observed ratios into A_V values, we have adopted the radiative transition probabilities given by Quinet et al. (1996) using the relativistic Hartree-Fock (HFR) computer programme. The extinction errors have been estimated directly from the flux error of each line. The results are reported in Table 3 for the individual knots where the S/N of the two lines is larger than 10.

A_V varies from ~ 6 in the knots Z1 and S to ~ 12 in the knot Z2. Fernandes (2000) found a value of $A_V = 9.38 \pm 1.49$ mag in a region that covers our knots HH46-1 and S. This value has however been derived employing the theoretical [Fe II] 1.644/1.257 μm ratio given by the radiative rates of Nussbaumer & Storey (1988) that predict higher values with respect to the Quinet et al. (1996) rates (Nisini et al. 2005). On the other hand, Antonucci et al. (2008) found an $A_V \sim 40$ mag on-source, indicating a high density gradient towards the central object. One should note here that the extinction found by Antonucci et al. (2008) on the basis of photometric measurements coupled with Bry emission is higher than the one we found on the knot S since [Fe II] lines trace more external regions. In addition, the knot S covers a region that extends $\sim 3''$ around the source position.

The extinction in the knot Z2 is roughly twice the extinction of the knots S and Z1. This fact could be due to the collision of the jet with stationary material on a side of the cavity. Heathcote et al. (1996) note the presence of an oblique shock due to the

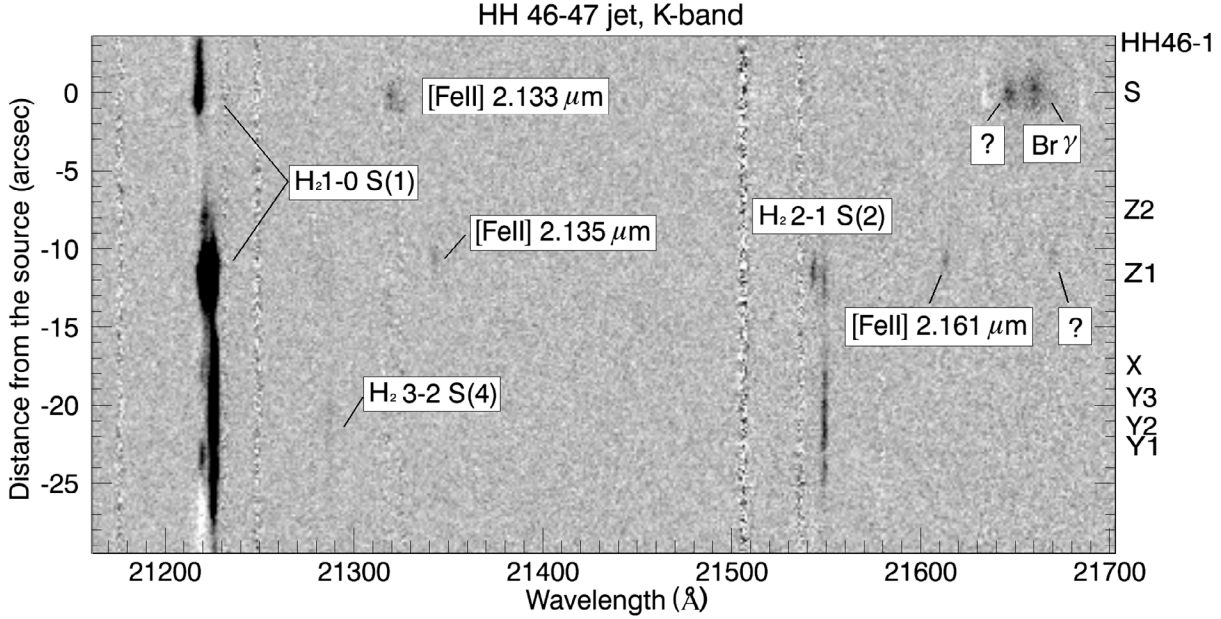


Fig. 3. MR continuum subtracted spectral image of the HH46-47 jet in the *K*-band. The distance from the source is represented on the left-hand *Y*-axis, while the knots are labelled on the right-hand *Y*-axis.

Table 3. A_V along the HH46-47 jet.

Knot	$A_V \pm \Delta A_V^a$ (mag)
] S	6.6 ± 0.2
Z2	12.5 ± 1.6
Z1	6.1 ± 0.1

Notes. ^(a) Visual extinction measured from the ratio [Fe II] 1.64/1.25 μm .

impact of the blue-shifted lobe of the jet with the cavity at $\sim 6''$ NE of the source. The same process may occur at the same distance in the red-shifted counter-lobe, giving rise to an increase in extinction.

5.2. H_2 temperature and mass flux

Using the different H_2 detected transitions, excitation diagrams for several knots (Z1, X, Y3, Y2 and Y1) along the jet showing enough H_2 lines have been constructed. As an example, Fig. 6 shows the excitation diagram of the knot Z1, the brightest knot observed in HH46-47. The excitation diagrams for the rest of the knots are reported in the Appendix B. In this kind of diagrams the natural logarithm of $N(\nu, J)/g_{\nu, J}$ versus the excitation energy $E(\nu, J)$ of a given level (ν, J) is represented, where $N(\nu, J)/g_{\nu, J}$ is the ratio of the column density over the statistical weight. The different symbols indicate lines coming from different vibrational levels, while the straight line represents the best linear fit through our data. The slope of the line is proportional to the inverse of the gas temperature. Extinction values as derived from the [Fe II] lines have been adopted. The extinction can, in principle, be also derived from the H_2 1-0S(1)/1-0Q(3) line ratio. But, this method involves lines close in wavelength and thus it is not sensitive enough to extinction variations. In addition, the Q lines fall in a poor atmospheric transition region (around $\sim 2.3 \mu\text{m}$) where their fluxes are affected by significant

uncertainties. Still, the fact that our data can be well traced by a straight line on the rovibrational diagram indicates that the extinction values derived from the [Fe II] lines agree well with the H_2 ones. The resulting temperature values are indicated in Table 4 and range between ~ 2000 K and ~ 2800 K.

The mass flux carried out by the warm molecular component (\dot{M}_{H_2}) has been also estimated from the observed H_2 transitions in the knots Z1, X, Y3, Y2 and Y1. \dot{M}_{H_2} can be inferred from the relationship $\dot{M}_{H_2} = 2 N(H_2) A dv_t/dl_t$. Here, A is the area of the emitting region sampled by the slit, dl_t and dv_t are the projected length and the tangential velocity, and $N(H_2)$ is the total column density. \dot{M}_{H_2} has been derived in the same spatial region extracted for the [Fe II] line analysis. The dv_t value has been taken from Eislöffel & Mundt (1994), while $N(H_2)$ for each knot has been found from the intercept to zero of the straight line fitted to the H_2 transitions in the Boltzmann diagram. The derived values for each knot are reported in Table 4. The average \dot{M}_{H_2} value along the jet is $\sim 3.8 \times 10^{-9} M_\odot \text{yr}^{-1}$. This estimate is however a lower limit, since we are only considering the warm component of the gas.

5.3. Electron density

The electron density (n_e) can be derived from [Fe II] lines coming from levels with similar excitation energies. This is the case of the ratio [Fe II] 1.600/1.644 μm , which is sensitive to n_e values between 10^3 – 10^5cm^{-3} and weakly dependent on the temperature. This ratio has been fitted with a NLTE code including the first 16 fine-structure levels of the [Fe II] (Nisini et al. 2002).

The electron density has been derived by integrating the total flux of the line profile of every extracted knot for both lines. The n_e values and the intervals used to extract the knots are reported in Table 5. Previous studies on protostellar jets like HH1, HH111 and HH34, have shown evidences of a decrease of the electron density with distance (see, e.g., Bacciotti & Eislöffel 1999; Nisini et al. 2005; Podio et al. 2006). The same behaviour may also occur in HH46-47. Indeed the electron density roughly decreases from a value of 6300cm^{-3} in knot S to a value of

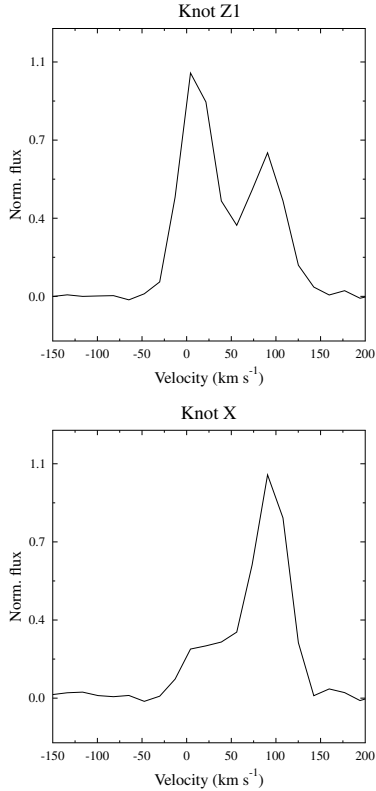


Fig. 4. Normalised line profiles of the H_2 2.122 μm line for knots Z1 (upper panel) and X (lower panel). In the X-axis the LSR radial velocity is represented. The velocities are corrected from a cloud velocity of $+20 \text{ km s}^{-1}$ (Hartigan et al. 1993)

3200 cm^{-3} in knot Z1. These two knots are displaced, however, in different lobes of the jet. In addition, the increase of n_e from knot Z2 to knot Z1 and the the lack of further [Fe II] emitting knots does not allow us to properly probe the dependence on distance of n_e .

5.4. [Fe II] depletion

Refractory species as iron are expected to be locked into dust grains in the quiescent conditions of molecular clouds. Still, high velocity shocks inside the jet beam are supposed to destroy the grains and release Fe atoms in gaseous form. In recent years several studies have been done to quantify the presence of dust along protostellar jets and measure the shock efficiency in disrupting the dust grain cores (see e.g., Nisini et al. 2005; Podio et al. 2006; Giannini et al. 2008). The iron gas phase abundance can be measured comparing the emission of [Fe II] with that of a non-refractory species of a known abundance. A very suitable ratio is the one between the [Fe II] 1.257 μm line and the [P II] 1.188 μm line (Oliva et al. 2001). These two lines are very close in wavelength and thus their ratio is poorly affected by extinction. In addition, both lines are excited under similar conditions and can be assumed in the first ionised state at a similar percentage. Assuming a solar abundance for both elements, the expected theoretical line ratio is $[\text{Fe II}]/[\text{P II}] \sim 1/2$ $[\text{Fe}/\text{P}] \sim 56$ (Oliva et al. 2001). Thus, observed values lower than this indicate that some of the iron is locked in grains.

Along the HH46-47 jet, both the [Fe II] 1.257 μm and the [P II] 1.188 μm lines have been detected in knots S and Z1. The measured $[\text{Fe II}]/[\text{P II}]$ ratio is ~ 7.3 in knot S and ~ 25.6 in

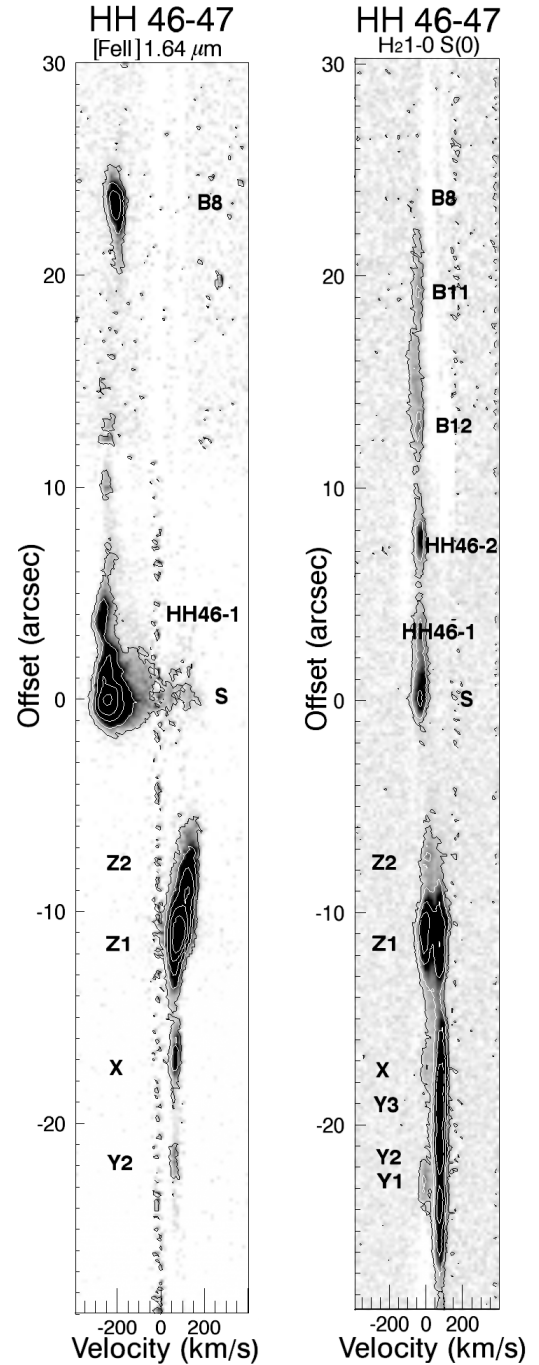


Fig. 5. Continuum-subtracted PVDs for the [Fe II] 1.644 μm and H_2 2.122 μm lines along the HH46-47 jet. Contours show values of 3, 9, ..., 243 σ for the [Fe II] line and 4.5, 13.5, ..., 364.5 σ for the H_2 . On the Y axis the distance from the source HH46-IRS is reported in arcsec.

knot Z1. These values indicate that around 88% and 58% of the iron is still in dust grains in knots S and Z1, respectively. This leads to a ratio $(\text{Fe}/\text{H})_{\text{gas}} \sim 3.92 \times 10^{-6}$ in the knot S and a $(\text{Fe}/\text{H})_{\text{gas}} \sim 1.18 \times 10^{-5}$ in the knot Z1. The strong iron depletion at the jet base is still lower than the 99% diffuse gas iron depletion (see, e.g., Savage & Sembach 1996), indicating that a small fraction of the iron has come back into gas phase at the base of the jet with respect to the interstellar value. Evidence that the gas phase iron abundance is low in knots close to the source and increases with the distance has been also found in the HH1 jet (Nisini et al. 2005). In knot Z1, the [Ti II] 1.140 μm line has also

Table 4. dv_t , T , $N(\text{H}_2)$, \dot{M}_{H_2} along the HH46-47 jet.

Knot	dv_t^a (km s^{-1})	T^b (K)	$N(\text{H}_2)^c$ (10^{17} cm^{-2})	$\dot{M}_{\text{H}_2}^d$ ($M_\odot \text{ yr}^{-1}$)
Z1	131	2797 ± 100	3.3	4.5×10^{-9}
X	19	2078 ± 42	3.7	7.3×10^{-10}
Y3	122	2564 ± 53	3.6	4.6×10^{-9}
Y2	122	2330 ± 50	5.1	6.4×10^{-9}
Y1	122	2093 ± 42	2.4	3.0×10^{-9}

Notes. ^(a) Tangential velocities from Eislöffel & Mundt (1994). ^(b) H_2 temperature. ^(c) H_2 column density. ^(d) H_2 mass ejection rate.

been detected. Ti is expected to be fully ionised in the jet plasma, since it has a low ionisation potential of 6.82 eV. Like iron, the titanium is a high-refractory element, and thus the Fe/Ti ratio can give us some clues about the relative abundance of both elements as well as about the selective depletion pattern of both elements in the dust along protostellar jets. With this aim we have computed the $[\text{Fe II}] 1.257 \mu\text{m}/[\text{Ti II}] 1.140 \mu\text{m}$ intensity ratio using an NLTE model for these species (Garcia Lopez et al. 2008). The observed ratio, assuming the physical conditions present in knot Z1 is ~ 70 , indicates a Fe/Ti ratio five times smaller than the one theoretically expected of $[\text{Fe/Ti}]_\odot = 354$, using the solar abundances of Asplund et al. (2005). The small Fe/Ti is consistent with what is found in the HH1 jet (Garcia Lopez et al. 2008), where a Fe/Ti ratio two to three times lower than solar was derived.

6. Medium resolution spectral analysis

6.1. Electron density and mass flux

The $[\text{Fe II}] 1.600$ and $1.644 \mu\text{m}$ lines have also been detected at medium resolution in the knots S, Z1 and Z2. In these knots we can test how the electron density varies as a function of the radial velocity by measuring the $1.600/1.644 \mu\text{m}$ ratio in each pixel along the spectral profile. The $[\text{Fe II}]$ ratio was computed only for the velocity points where the intensity is greater than $S/N \sim 3$. Figure 7 shows electron density variations along the MR spectral profile of the knots S, Z1 and Z2 (upper panels) together with the normalised line profile of the $[\text{Fe II}] 1.600 \mu\text{m}$ and $1.644 \mu\text{m}$ lines (lower panels). The electron density increases as the velocity decreases in all of the knots where two velocity components were detected in $[\text{Fe II}]$. In particular, the knot S close to the source has a behaviour very similar to what was found in HH34 (Garcia Lopez et al. 2008), with the electron densities higher in the gas at low velocity. We have separately measured the n_e in the HVC and LVC components. Near to the source (knot S), we have defined a HVC ranging from $\sim 239 \text{ km s}^{-1}$ to $\sim 181 \text{ km s}^{-1}$ (consistent with the FWHM of a Gaussian-fit through the line), and an LVC from $\sim 181 \text{ km s}^{-1}$ to $\sim 50 \text{ km s}^{-1}$. Far from the source, only the knot Z2 shows a clear double velocity component: here we have defined the intervals from $\sim 110 \text{ km s}^{-1}$ to $\sim 167 \text{ km s}^{-1}$ and from $\sim 80 \text{ km s}^{-1}$ to $\sim 110 \text{ km s}^{-1}$ for the high and low velocity gas, respectively.

The n_e values for the integrated velocity components are reported in Table 5. The electron density of the LVC ($n_e(\text{LVC}) \sim 4600\text{--}7600$) is higher than the electron density of the HVC ($n_e(\text{HVC}) \sim 2300\text{--}5000$) as evidenced by Fig. 7. The behaviour found in knot S is similar to what we have already found at the HH34 jet base and contrasts with the results for T Tauri

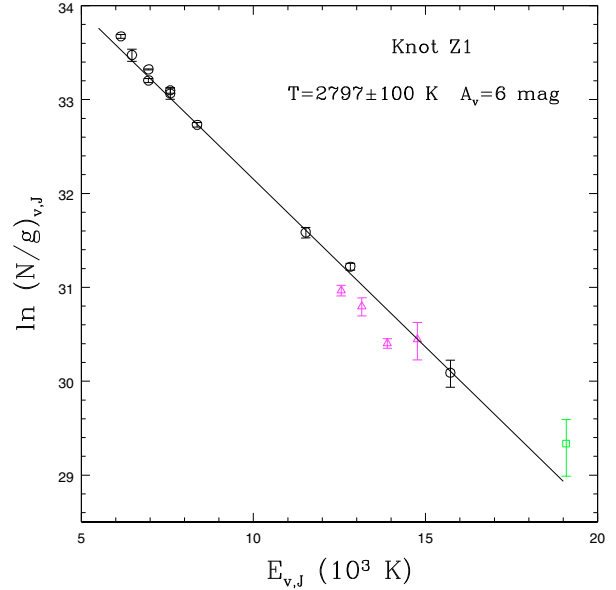


Fig. 6. H_2 rotational diagram for the different lines in the knot Z1 of HH46-47. Different symbols indicate lines coming from different vibrational levels: circles indicate $v = 1$, triangles $v = 2$ and squares $v = 3$. The straight line represents the best fit through the data. The corresponding temperature and the adopted extinction value is indicated.

stars, where the highest electron density is associated with the high velocity gas pertaining to the more collimated inner jet section, while the low velocity component is a less collimated gas at lower density (e.g., Coffey et al. 2008). These contrasting results may reflect different excitation conditions in the structure of Class I jets or may be a result biased by the low spatial resolution of our observations that does not allow us to resolve the same spatial scales as those probed in T Tauri jets, namely within 100–200 AU.

At the bow shock positions far from the source, like in the Z2 knot, variations of the electron density with velocity may depend on the bow inclination angle and the section of the bow intercepted by the slit, as shown by Indebetouw & Noriega-Crespo (1995). According to this model, a bow shock seen on-axis at an inclination angle of ~ 30 degree, as in our case, shows qualitatively a behaviour like the one we observe, namely with the highest electron densities displaced at low velocity.

In order to compute the contribution to the mass flux of the atomic component, we have derived \dot{M}_{jet} from the luminosity of the $[\text{Fe II}] 1.644 \mu\text{m}$ line, following the approach described in Garcia Lopez et al. (2008). To compute the theoretical $[\text{Fe II}]$ lines fractional population, the n_e values derived separately for the LV and HV components have been assumed. A constant value of 10 000 K have instead been assumed for the electron temperature: the derived populations are only a little sensitive to this value and the results do not change significantly if the temperature is maintained between ~ 7000 K and 15 000 K. An inclination angle of the jet with respect to the plane of the sky $i \sim 34^\circ$ (Eislöffel & Mundt 1994) has been assumed and used to infer the velocity of the knots projected perpendicular to the line of sight through our measurements of the radial velocity. These values are reported in Table 6, while the adopted length of the knots projected perpendicular to the line of sight is listed in Table 5. The $[\text{Fe II}] 1.644 \mu\text{m}$ line flux has been de-reddened using the extinction derived from the ratio $[\text{Fe II}] 1.644/1.257$ and reported in Table 3.

Table 5. Electron density along the HH46-47 jet.

Knot	r_t^a ($''$)	$n_e \pm \Delta n_e^b$ (cm^{-3})	$n_e(\text{HVC})^c$ (cm^{-3})	$n_e(\text{LVC})^b$ (cm^{-3})
S	(-3.4, +2.8)	6300^{+1700}_{-1300}	5400	7650
Z2	(-9.3, -5)	1300^{+1800}_{-1200}	2350	4600
Z1	(-14.8, -9.3)	3200^{+700}_{-850}	3100	

Notes. ^(a) Distance from the source in arcsec. Negative values correspond to the southeastern, redshifted jet axis. ^(b) Electron density measured from the ratio [Fe II] 1.60/1.64 μm . ^(c) Electron density measured from the ratio [Fe II] 1.60/1.64 μm for the HVC and LVC.

Table 6. \dot{M}_{jet} along the HH46-47 jet.

Knot	$dv_t(\text{HVC})^a$	$\dot{M}_{\text{jet}}(\text{HVC})^b$	$dv_t(\text{LVC})^a$	$\dot{M}_{\text{jet}}(\text{LVC})^b$
	km s^{-1}	$10^{-7} M_{\odot} \text{yr}^{-1}$	km s^{-1}	$10^{-8} M_{\odot} \text{yr}^{-1}$
S	316	0.3–1.9	205	0.5–3.6
Z2	213	0.4–0.9	136	0.2–0.4
Z1	166	0.4–1.0		

Notes. ^(a) Tangential velocity derived from the observed radial velocities assuming an orientation angle of the jet with respect to the plane of the sky of 34° (Eislöffel & Mundt 1994). ^(b) \dot{M}_{jet} measured from the luminosity of the [Fe II] 1.64 μm for the HVC and LVC. The lower value has been derived assuming an iron solar abundance, while the upper value has been inferred assuming the iron gas-phase abundance derived from the [Fe II]/[P II] ratio.

\dot{M}_{jet} values have been derived both assuming a solar abundance of iron and considering the gas-phase Fe abundance measured from the Fe/P analysis, in the assumption that the same dust depletion factor is valid for both the HVC and LVC. The corresponding range of values are listed in Table 6. Values of the order of $0.5\text{--}1 \times 10^{-7} M_{\odot} \text{yr}^{-1}$ are found in the HVC, while the LVC shows ~ 16 times lower values.

7. Discussion

The [Fe II] and H_2 emission structure at the base of HH46-47 is very similar to the one observed in several Class I jets (e.g., Davis et al. 2001b, 2003; Takami et al. 2006). As in the case of CTTS jets, the forbidden-emission line (FEL) regions of Class I jets are characterised by the presence of two velocity components at the jet base at high and low velocity. The MHFL regions as traced by H_2 emission show on contrast just a LVC near the source while higher velocity H_2 is usually detected further downstream. In particular the kinematics and physical parameters of the HH46-47 jet are very similar to those found in our previous work on HH34 (García Lopez et al. 2008), where the physical properties have also been derived as a function of velocity. For instance, Fig. 8 shows the [Fe II] 1.644 μm PVDs of the inner region of these two jets. Since the two objects are at a similar distance (i.e. 450 pc), the emission regions have the same physical extent in this figure. In both the PVDs, the [Fe II] lines broaden and emission at lower velocities down to 0 km s^{-1} appears within $\sim 2''$ from the central source, i.e. up to distances of $\sim 1000 \text{ AU}$. The extent of the LVC is comparable with the typical size of the envelope of Class I sources (see, e.g., Andre & Montmerle 1994). Thus this result may indicate an interaction of a low-velocity disc-wind with the source envelope as the possible origin of the LVC in Class I jets. The large extent of the LVC

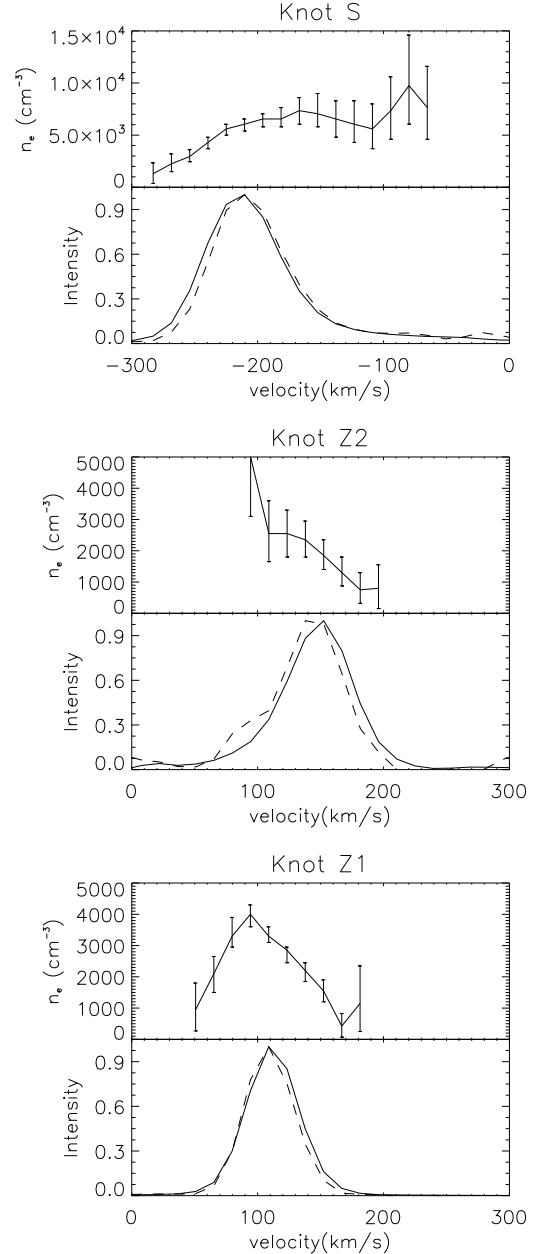


Fig. 7. Normalised to one line profiles (*lower panels*) of the [Fe II] lines 1.644 μm (solid line) and 1.600 μm (dotted line), and the electron density in each velocity channel (*upper panels*) for different extracted knots along the HH46-47 jet.

is at variance with the PVDs of most of the CTT, where the LVC is usually confined within $\sim 200 \text{ AU}$ from the source (Pyo et al. 2003, 2006).

The values of electron density and mass flux rate that we derive in HH46-47 and their dependence on the velocity are also similar to those inferred on HH34, i.e., $n_e \sim 0.5\text{--}1 \times 10^4 \text{ cm}^{-3}$ in the HVC and $\sim 1\text{--}2 \times 10^4 \text{ cm}^{-3}$ in the LVC, and \dot{M}_{jet} of the order $10^{-7} M_{\odot} \text{yr}^{-1}$. Similar values have also been estimated on a number of Class I YSO jets (e.g., Davis et al. 2003; Podio et al. 2006; Takami et al. 2006).

At variance with [Fe II], the H_2 PVDs of HH46-47 shows a different behaviour with respect to the one of HH34. In HH34 the H_2 PVD shows spatially- and kinematically-separated LVC and HVC, and only the LVC is visible down to the central source. In HH46-47, on the contrary, a single velocity component near the

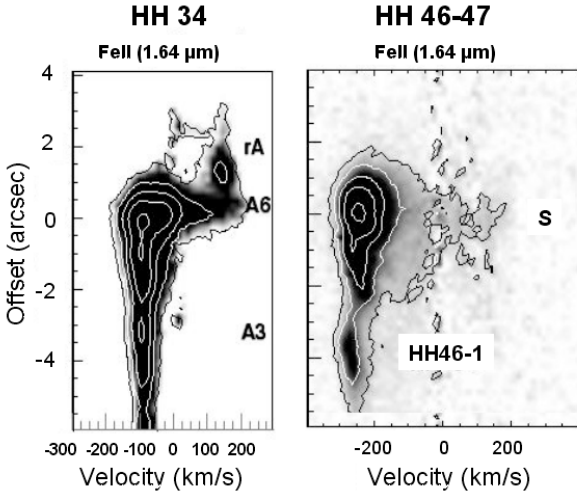


Fig. 8. PVD of the [Fe II] 1.644 μm line for the HH34 and HH46-47 jets.

source is detected. The morphology and kinematics of the H_2 close to the source (the MHEL regions; Davis et al. 2001b) in Class I objects varies indeed significantly from source to source (Davis et al. 2001b, 2002) and this is another element that makes the origin of the MHEL regions unclear.

In Garcia Lopez et al. (2008) we have compared the [Fe II] 1.644 μm PVDs of HH34 with those of the synthetic PVDs available for the disc-wind and X-wind models (Pesenti et al. 2004; Shang et al. 1998). Most of this discussion is also valid for the HH46-47 jet. Briefly, none of these models are able to explain the persistency of the LVC at large distances from the launching regions. This may suggest that the low velocity that we observe far from the source represents dense gas entrained by the high-velocity collimated jet rather than directly ejected gas from the acceleration region.

From the observed HH46-47 peak radial velocity of the HVC, corrected for the inclination angle, we estimate a jet poloidal velocity around 350 km s^{-1} . This value is just at the border of the range of poloidal velocities predicted by X-wind models and it also agrees with disc-wind models with launching radii in the range of 0.07–0.15 AU and magnetic lever arms larger than ~ 5 (Ferreira et al. 2006).

Further constraints on MHD launching models may be derived from the presence of dust in the initial beam of the HH46-47 jet, as suggested by Podio et al. (2009). We have in fact seen that around 88% of the iron within 450 AU from the source is depleted, implying that a large fraction of dust grains are still present at the jet base. Dust grains of the ambient medium are expected to be destroyed by the passage of the initial leading bow-shock that has velocities higher than 100 km s^{-1} (Draine 2003). Since the amount of iron depletion decreases toward the external knots (only 58% of iron is found to be depleted in grains at ~ 5000 AU from the source), dust grains are unlikely to come from entrained material. In addition they cannot be reformed along the jet beam since the time required for grain reformation is $\sim 10^7$ – 10^8 yr (Jones 2001), while the jet takes ~ 1300 yr to travel from the central source to the final bow-shock (Hartigan et al. 2005). Therefore, the larger amount of grains near the source may suggest that they have been removed from the accretion disc and transported through the jet. Interestingly it has been shown that in the case of Herbig stars and T Tauri stars the disc is populated by dust grains only beyond the so-called dust evaporation point, R_{evp} (Akeson et al. 2005; Eisner et al. 2007b,a).

Future similar measurements of R_{evp} for Class 0/I sources would help to constrain the region from which dusty jets are launched.

8. Conclusions

We have presented medium resolution (MR) (in the H - and K -band) and low resolution (LR) (in the J -, H - and K -band) spectra of the Class I driven HH46-47 jet. These observations allow us to resolve two velocity components at the jet base and to study the kinematics and physical properties of the jet as a function of velocity. From the [Fe II] 1.644/1.600 μm lines the electron density has been derived along the jet and as a function of velocity. In addition, from the luminosity of the [Fe II] 1.644 μm line the mass flux for the different velocity components has been derived. Finally, the [Fe II]/[P II] ratio has been used to retrieve important information about the dust depletion inside the jet beam. We summarise our results as follows:

- We were able to trace the HH46-47 jet down to the central source. While the atomic component shows a HVC and LVC near the source, only a single velocity component has been detected for the molecular gas. Within $1''$ from the source, the atomic emission broadens down to 0 km s^{-1} and even reaches red-shifted velocities.
- From the ratio of the [Fe II] 1.644, 1.257 μm lines detected in the LR spectra, the visual extinction for different knots have been derived. We have found an A_V ranging from ~ 6 mag to ~ 12 mag along the jet.
- Several H_2 lines have been detected from the LR spectra, allowing us to construct excitation diagrams for different knots. From these diagrams we have derived the temperature and mass flux for the warm molecular component of the jet. The temperature has an average value around ~ 2300 K, while we have found an average mass flux for the warm molecular component of $\geq 3.7 \times 10^{-9} M_{\odot} \text{ yr}^{-1}$.
- The electron density, derived from the [Fe II] 1.600/1.644 μm ratio, roughly decreases from the internal to the more external knots from 9400 to 3200 cm^{-3} . Larger electron density values are found in the LVC with respect to the HVC for all the extracted knots, with an average value of ~ 6000 and $\sim 4000 \text{ cm}^{-3}$ for the LVC and HVC, respectively.
- From the [Fe II]/[P II] ratio, we have estimated the iron depletion in the knots S and Z1. We have found that around 88% and 58% of the iron is depleted in grains in the knot S and Z1.
- The mass flux rate transported by the [Fe II] has been derived for both the velocity components assuming the Fe gas-phase abundance derived in this paper. We found that the HVC is transporting the bulk of the mass along the jet with average values of $\dot{M}_{\text{jet}}(\text{HVC}) \sim 1.2 \times 10^{-7} M_{\odot} \text{ yr}^{-1}$ and $\dot{M}_{\text{jet}}(\text{LVC}) \sim 2 \times 10^{-8} M_{\odot} \text{ yr}^{-1}$. As in the case of HH34 (Garcia Lopez et al. 2008), the difference in the tangential velocity between the HVC and LVC is not enough to account for the much higher \dot{M}_{jet} value in the HVC, indicating a significantly larger value of the $(n_{\text{H}}V)^4$ product in the HVC than in the LVC (from a factor ~ 1.5 in the knot Z2 to ~ 3.5 in knot S).
- Many of the derived properties of the HH46-47 are common to jets from YSOs in different evolutionary states. The derived densities and mass flux values are typical of Class I objects or very active T Tauri stars. However, the observed spatial extent of the LVC and the velocity dependence of the

⁴ Where n_{H} and V are the total density and the emitting volume, see Garcia Lopez et al. (2008) for more details.

electron density are not explained by the current jet formation models.

Acknowledgements. The present work was partly supported by the European Communitys Marie Curie Actions – Human Resource and Mobility within the JETSET (Jet Simulations, Experiments and Theory) network under contract MRTN-CT-2004 005592. L.P. work was funded by a Fellowship from the Irish Research Council for Science, Engineering and Technology.

References

- Akeson, R. L., Boden, A. F., Monnier, J. D., et al. 2005, *ApJ*, 635, 1173
 Andre, P., & Montmerle, T. 1994, *ApJ*, 420, 837
 Antonucci, S., Nisini, B., Giannini, T., & Lorenzetti, D. 2008, *A&A*, 479, 503
 Asplund, M., Grevesse, N., & Sauval, A. J. 2005, in *Cosmic Abundances as Records of Stellar Evolution and Nucleosynthesis*, ed. T. G. Barnes, III, & F. N. Bash, ASP Conf. Ser., 336, 25
 Bacciotti, F., & Eisloffel, J. 1999, *A&A*, 342, 717
 Bacciotti, F., Mundt, R., Ray, T. P., et al. 2000, *ApJ*, 537, L49
 Coffey, D., Bacciotti, F., & Podio, L. 2008, *ApJ*, 689, 1112
 Davis, C. J., Hodapp, K. W., & Desroches, L. 2001a, *A&A*, 377, 285
 Davis, C. J., Ray, T. P., Desroches, L., & Aspin, C. 2001b, *MNRAS*, 326, 524
 Davis, C. J., Stern, L., Ray, T. P., & Chrysostomou, A. 2002, *A&A*, 382, 1021
 Davis, C. J., Whelan, E., Ray, T. P., & Chrysostomou, A. 2003, *A&A*, 397, 693
 Davis, C. J., Nisini, B., Takami, M., et al. 2006, *ApJ*, 639, 969
 Draine, B. T. 2003, *ARA&A*, 41, 241
 Eisloffel, J., & Mundt, R. 1994, *A&A*, 284, 530
 Eisloffel, J., Davis, C. J., Ray, T. P., & Mundt, R. 1994, *ApJ*, 422, L91
 Eisner, J. A., Chiang, E. I., Lane, B. F., & Akeson, R. L. 2007a, *ApJ*, 657, 347
 Eisner, J. A., Hillenbrand, L. A., White, R. J., et al. 2007b, *ApJ*, 669, 1072
 Fernandes, A. J. L. 2000, *MNRAS*, 315, 657
 Ferreira, J. 1997, *A&A*, 319, 340
 Ferreira, J., Dougados, C., & Cabrit, S. 2006, *A&A*, 453, 785
 Garcia Lopez, R., Nisini, B., Giannini, T., et al. 2008, *A&A*, 487, 1019
 Giannini, T., Calzoletti, L., Nisini, B., et al. 2008, *A&A*, 481, 123
 Hartigan, P., Morse, J. A., Heathcote, S., & Cecil, G. 1993, *ApJ*, 414, L121
 Hartigan, P., Heathcote, S., Morse, J. A., Reipurth, B., & Bally, J. 2005, *AJ*, 130, 2197
 Heathcote, S., Morse, J. A., Hartigan, P., et al. 1996, *AJ*, 112, 1141
 Indebetouw, R., & Noriega-Crespo, A. 1995, *AJ*, 109, 752
 Jones, A. P. 2001, *Roy. Soc. London Philos. Trans. Ser. A*, 359, 1961
 Lavalley, C., Cabrit, S., Dougados, C., Ferruit, P., & Bacon, R. 1997, *A&A*, 327, 671
 Nishikawa, T., Takami, M., Hayashi, M., Wiseman, J., & Pyo, T.-S. 2008, *ApJ*, 684, 1260
 Nisini, B., Caratti o Garatti, A., Giannini, T., & Lorenzetti, D. 2002, *A&A*, 393, 1035
 Nisini, B., Bacciotti, F., Giannini, T., et al. 2005, *A&A*, 441, 159 (N05)
 Nussbaumer, H., & Storey, P. J. 1988, *A&A*, 193, 327
 Oliva, E., Marconi, A., Maiolino, R., et al. 2001, *A&A*, 369, L5
 Presenti, N., Dougados, C., Cabrit, S., O'Brien, D., & Garcia, P. J. V. 2004, *Ap&SS*, 292, 539
 Podio, L., Bacciotti, F., Nisini, B., et al. 2006, *A&A*, 456, 189 (P06)
 Podio, L., Medves, S., Bacciotti, F., Eisloffel, J., & Ray, T. P. 2009, *A&A*, 506, 779
 Pyo, T.-S., Kobayashi, N., Hayashi, M., et al. 2003, *ApJ*, 590, 340
 Pyo, T.-S., Hayashi, M., Kobayashi, N., et al. 2006, *ApJ*, 649, 836
 Quinet, P., Le Dourneuf, M., & Zeippen, C. J. 1996, *A&AS*, 120, 361
 Reipurth, B., Yu, K. C., Heathcote, S., Bally, J., & Rodríguez, L. F. 2000, *AJ*, 120, 1449
 Savage, B. D., & Sembach, K. R. 1996, *ApJ*, 470, 893
 Schultz, A. S. B., Burton, M. G., & Brand, P. W. J. L. 2005, *MNRAS*, 358, 1195
 Shang, H., Shu, F. H., & Glassgold, A. E. 1998, *ApJ*, 493, L91
 Shu, F. H., Najita, J., Ostriker, E. C., & Shang, H. 1995, *ApJ*, 455, L155
 Takami, M., Chrysostomou, A., Ray, T. P., et al. 2006, *ApJ*, 641, 357

Appendix A: Knot fluxes at low resolution**Table A.1.** Observed unreddened lines along HH46-47: atomic lines.

Line id.	$\lambda(\mu\text{m})$	$F(\Delta F)(10^{-16} \text{ erg s}^{-1} \text{ cm}^{-2})$				
		S	HH46-1	B8	Z2	X
[P II] $^3\text{P}_2-^1\text{D}_2$	1.188	6.2(1.2)
[Fe II] $\text{a}^4\text{D}_{5/2}-\text{a}^6\text{D}_{7/2}$	1.249	1.9(0.6)
[Fe II] $\text{a}^4\text{D}_{7/2}-\text{a}^6\text{D}_{9/2}$	1.257	54.2(0.8)	15.8(0.9)	11.9(0.7)	7.1(0.9)	6.4(1.0)
[Fe II] $\text{a}^2\text{G}_{9/2}-\text{a}^4\text{D}_{7/2}$	1.267	3.2(0.8)
[Fe II] $\text{a}^4\text{D}_{1/2}-\text{a}^6\text{D}_{1/2}$	1.271	2.0(0.3)
[Fe II] $\text{a}^4\text{D}_{3/2}-\text{a}^6\text{D}_{3/2}$	1.279	2.4(0.6)
[Fe II] $\text{a}^4\text{D}_{5/2}-\text{a}^6\text{D}_{5/2}$	1.295	8.9(1.1)
[Fe II] $\text{a}^4\text{D}_{3/2}-\text{a}^6\text{D}_{1/2}$	1.298	3.4(0.9)
[Fe II] $\text{a}^2\text{G}_{7/2}-\text{a}^4\text{D}_{3/2}$	1.300	1.7(0.6)
[Fe II] $\text{a}^4\text{D}_{7/2}-\text{a}^6\text{D}_{7/2}$	1.321	13.1(0.4)	4.5(1.4)	3.5(0.5)	3.0(1.2)	2.4(1.2)
[Fe II] $\text{a}^4\text{D}_{5/2}-\text{a}^6\text{D}_{3/2}$	1.328	4.3(0.6)
[Fe II] $\text{a}^4\text{D}_{5/2}-\text{a}^4\text{F}_{9/2}$	1.534	9.9(1.0)	0.7(0.4)	...
[Fe II] $\text{a}^4\text{D}_{3/2}-\text{a}^4\text{F}_{7/2}$	1.600	11.2(1.0)	0.9(0.4)	...
[Fe II] $\text{a}^4\text{D}_{7/2}-\text{a}^4\text{F}_{9/2}$	1.644	85.8(0.7)	8.9(0.5)	8.7(0.8)	20.1(0.5)	4.4(0.5)
[Fe II] $\text{a}^4\text{D}_{1/2}-\text{a}^4\text{F}_{5/2}$	1.664	5.7(0.8)	1.1(0.7)	...
[Fe II] $\text{a}^4\text{D}_{5/2}-\text{a}^4\text{F}_{7/2}$	1.677	13.3(0.9)	1.8(0.4)	...
[Fe II] $\text{a}^4\text{D}_{3/2}-\text{a}^4\text{F}_{3/2}$	1.797	5.2(0.9)
[Fe II] $\text{a}^4\text{D}_{5/2}-\text{a}^4\text{F}_{5/2}$	1.800	14.3(0.7)
[Fe II] $\text{a}^4\text{D}_{7/2}-\text{a}^4\text{F}_{7/2}$	1.810	52.6(1.1)
[Fe II] $\text{a}^2\text{P}_{3/2}-\text{a}^4\text{P}_{3/2}$	2.133	3.2(0.5)

Table A.2. Observed unreddened lines along HH46-47: H₂ lines.

Line id.	$\lambda(\mu\text{m})$	$F(\Delta F)(10^{-16} \text{ erg s}^{-1} \text{ cm}^{-2})$					
		S	Z2	X	Y3	Y2	Y1
H ₂ 2-1 S(5)	1.945	2.7(0.7)
H ₂ 1-0 S(2)	2.034	...	2.1(0.6)	26.6(0.6)	10.0(0.6)	13.2(0.4)	8.7(0.4)
H ₂ 2-1 S(3)	2.074	3.7(0.5)	2.3(0.2)	3.9(0.4)	...
H ₂ 1-0 S(1)	2.122	12.0(0.5)	5.6(0.3)	36.3(0.3)	27.0(0.3)	3.3(0.2)	22.7(0.2)
H ₂ 2-1 S(2)	2.154	1.1(0.2)	...	1.6(0.2)	...
H ₂ 1-0 S(0) ^a	2.224	12.7(0.6)	3.1(0.6)	7.7(0.4)	5.4(0.5)	6.9(0.3)	5.2(0.2)
H ₂ 2-1 S(1)	2.248	...	1.4(0.4)	3.4(0.3)	3.0(0.5)	4.6(0.2)	3.5(0.3)
H ₂ 1-0 Q(1)	2.407	16.6(1.3)	4.8(0.6)	28.9(0.6)	20.8(0.8)	24.3(0.7)	17.8(0.5)
H ₂ 1-0 Q(2)	2.413	13.8(1.5)	2.3(0.3)
H ₂ 1-0 Q(3)	2.424	16.2(1.3)	5.8(0.5)	30.7(0.6)	23.3(1.5)	26.5(0.7)	17.8(0.5)
H ₂ 1-0 Q(4)	2.437	9.3(1.1)	...	8.4(0.7)	6.1(1.2)	8.0(0.6)	5.2(0.6)
H ₂ 1-0 Q(5)	2.455	23.4(0.9)	15.7(1.6)	21.6(0.8)	14.9(0.7)
H ₂ 1-0 Q(6)	2.476	6.6(0.6)	...

Notes. ^(a) Blend with [Fe II] $\text{b}^2\text{F}_{5/2}-\text{a}^2\text{F}_{7/2}$.

Appendix B: Rovibrational diagrams

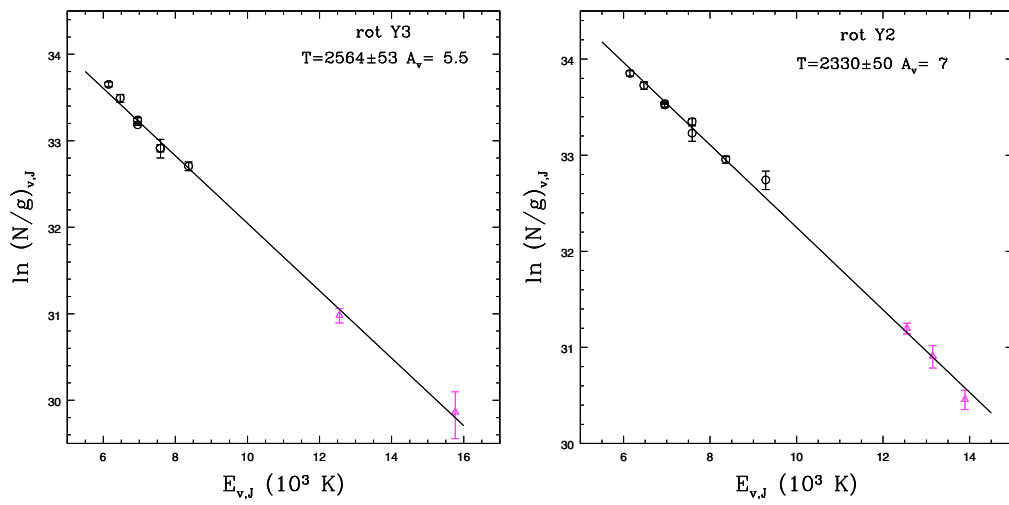


Fig. B.1. As Fig. 6 for knot Y3 and knot Y2.

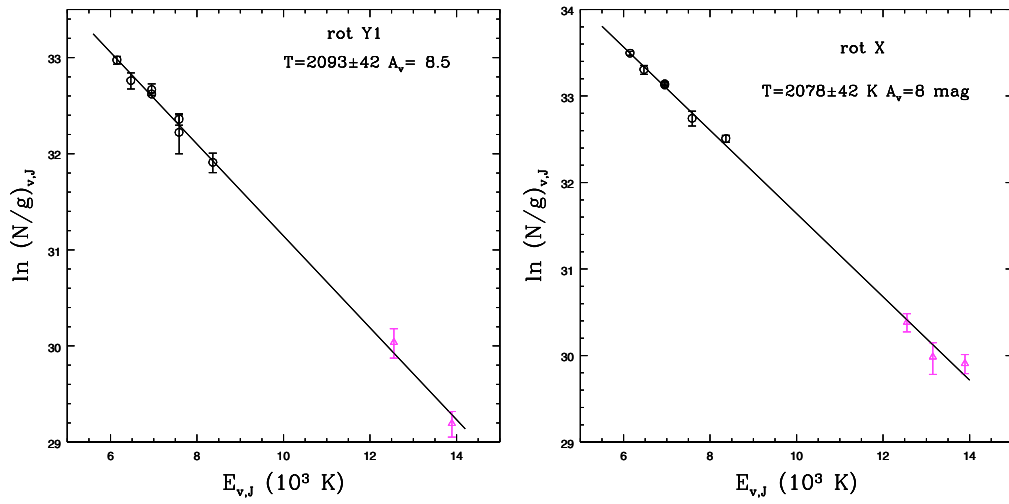


Fig. B.2. As Fig. 6 for knot Y1 and knot X.